

Figure 5 Second-quadrant B - H curves for the annealed samples. **a**, An annealed 4 nm $\text{Fe}_{58}\text{Pt}_{42}$ nanoparticle assembly. **b**, A hard-soft exchange-coupled FePt - Fe_3Pt nanocomposite. The composite was obtained from the annealed Fe_3O_4 (4 nm): $\text{Fe}_{58}\text{Pt}_{42}$ (4 nm) assembly (mass ratio Fe_3O_4 : FePt = 1:10). The energy product, $(BH)_{\text{max}}$, describes the available energy density of the materials and is defined as the maximum BH product of the second-quadrant B - H curve²¹.

The optimized nanostructures for exchange coupling yield both high remanent magnetization and coercivity, resulting in an enhanced energy product $(BH)_{\text{max}}$ (ref. 21). Figure 5 illustrates B - H curves of an annealed 4 nm $\text{Fe}_{58}\text{Pt}_{42}$ nanoparticle assembly (Fig. 5a), and a nanocomposite from a Fe_3O_4 (4 nm): $\text{Fe}_{58}\text{Pt}_{42}$ (4 nm) assembly with a 1:10 mass ratio (Fig. 5b). The measured $(BH)_{\text{max}}$ for the single-phase $\text{Fe}_{58}\text{Pt}_{42}$ is 14.7 MG Oe. For the nanocomposite derived from Fe_3O_4 (4 nm): $\text{Fe}_{58}\text{Pt}_{42}$ (4 nm) assembly, $(BH)_{\text{max}}$ reaches 20.1 MG Oe, exceeding the value for single phase $\text{Fe}_{58}\text{Pt}_{42}$ assembly by 37%, and the theoretical limit of 13 MG Oe for non-exchange-coupled isotropic FePt by over 50%. This $(BH)_{\text{max}}$ enhancement clearly indicates effective exchange coupling between the hard and soft phases.

We have described the fabrication of exchange-coupled isotropic FePt - Fe_3Pt nanocomposite magnets by self-assembly of binary FePt and Fe_3O_4 nanoparticles, and controlled annealing. By engineering the nanoscale dimension and spatial distribution of the hard and soft phases, an enhanced energy product is achieved. Our approach shows great potential for future fabrication of high-performance exchange-spring magnets. Further, it can be extended to other multi-component systems, providing both a model for studying fundamental relationships between nanostructure and interparticle interactions, and a practical route to functional nanocomposites and devices. □

Received 15 July; accepted 10 October 2002; doi:10.1038/nature01208.

- Kneller, E. F. & Hawig, R. The exchange-spring magnet: a new material principle for permanent magnets. *IEEE Trans. Magn.* **27**, 3588–3600 (1991).
- Skomski, R. & Coey, J. M. D. Giant energy product in nanostructured two-phase magnets. *Phys. Rev. B* **48**, 15812–15816 (1993).
- Schrefl, T., Kronmüller, H. & Fidler, J. Exchange hardening in nano-structured two-phase permanent magnets. *J. Magn. Mater.* **127**, L273–L277 (1993).
- Coehoorn, R., De Mooij, D. B. & De Waard, C. Melt-spun permanent magnet materials containing Fe_3B as the main phase. *J. Magn. Mater.* **80**, 101–104 (1989).
- Ping, D. H., Hono, K. & Hirotsawa, S. Partitioning of Ga and Co atoms in a $\text{Fe}_3\text{B}/\text{Nd}_2\text{Fe}_{14}\text{B}$ nanocomposite magnet. *J. Appl. Phys.* **83**, 7769–7775 (1998).
- Kobayashi, T., Yamasaki, M. & Hamano, M. Mössbauer study on intergranular phases in the bcc- Fe/NdFeB nanocomposite alloys. *J. Appl. Phys.* **87**, 6579–6581 (2000).
- Gong, W., Hadjipanayis, G. C. & Krause, R. F. Mechanically alloyed nanocomposite magnets. *J. Appl. Phys.* **75**, 6649–6651 (1994).
- McCormick, P. G. et al. Mechanically alloyed nanocomposite magnets. *J. Appl. Phys.* **83**, 6256–6261 (1998).
- Zhang, J., Zhang, S.-Y., Zhang, H.-W., Shen, B.-G. & Li, B.-H. Structure and magnetic properties of $\text{Sm}_2\text{Co}_2/\alpha\text{-Fe}$ ($x = 0.65$ – 1.3) prepared by mechanical milling and subsequent annealing. *J. Appl. Phys.* **89**, 2857–2860 (2001).
- Fullerton, E. E., Jiang, J. S., Sowers, C. H., Pearson, J. E. & Bader, S. D. Structure and magnetic properties of exchange-spring Sm-Co/Co superlattices. *Appl. Phys. Lett.* **72**, 380–382 (1997).
- Liu, J. P., Luo, C. P., Liu, Y. & Sellmyer, D. J. High energy products in rapidly annealed nanoscale FePt multilayers. *Appl. Phys. Lett.* **72**, 483–485 (1998).

- Liu, J. P., Liu, Y., Skomski, R. & Sellmyer, D. J. Magnetic hardening in SmCo_5 - Co multilayers and nanocomposites. *J. Appl. Phys.* **85**, 4812–4814 (1999).
- Sun, S., Murray, C. B., Weller, D., Folks, L. & Moser, A. Monodisperse FePt nanoparticles and ferromagnetic FePt nanocrystal superlattices. *Science* **287**, 1989–1992 (2000).
- Sun, S., Fullerton, E. E., Weller, D. & Murray, C. B. Compositionally controlled FePt nanoparticle materials. *IEEE Trans. Magn.* **37**, 1239–1243 (2001).
- Sun, S. & Zeng, H. Size controlled synthesis of magnetic nanoparticles. *J. Am. Chem. Soc.* **124**, 8204–8205 (2002).
- Kiely, C. J., Fink, J., Brust, M., Bethell, D. & Schiffrin, D. J. Spontaneous ordering of bimodal ensembles of nanoscopic gold clusters. *Nature* **396**, 444–446 (1998).
- Weller, D. et al. High K_u materials approach to 100 Gbits/in². *IEEE Trans. Magn.* **36**, 10–15 (2000).
- Klemmer, T., Hoydick, D., Okumura, H., Zhang, B. & Soffa, W. A. Magnetic hardening and coercivity mechanisms in L1_0 ordered FePd ferromagnets. *Scripta Met.* **33**, 1793–1805 (1995).
- Podgorny, M. Electronic structure of the ordered phases of Pt-Fe alloys. *Phys. Rev. B* **43**, 13700–13718 (1991).
- Zeng, H. et al. Exchange-coupled FePt nanoparticle assembly. *Appl. Phys. Lett.* **80**, 2583–2585 (2002).
- O’Handley, R. C. *Modern Magnetic Materials* 469–472 (John Wiley & Sons, New York, 2000).

Acknowledgements This work is supported in part by the US Defense Advanced Research Program Agency (DARPA) through the Army Research Office (ARO). H. Z. and J. L. thank DARPA for support through Louisiana Tech University.

Competing interests statement The authors declare that they have no competing financial interests.

Correspondence and requests for materials should be addressed to S.S. (e-mail: ssun@us.ibm.com).

Active transport of Ca^{2+} by an artificial photosynthetic membrane

Ira M. Bennett*, Hebe M. Vanegas Farfano*, Federica Bogani*, Alex Primak*, Paul A. Liddell*, Luis Otero†, Leonides Sereno†, Juana J. Silber†, Ana L. Moore*, Thomas A. Moore* & Devens Gust*

* Department of Chemistry and Biochemistry and Center for the Study of Early Events in Photosynthesis, Arizona State University, Tempe, Arizona 85287, USA
 † Departamento de Química y Física, Universidad Nacional de Río Cuarto, Río Cuarto, Argentina

Transport of calcium ions across membranes and against a thermodynamic gradient is essential to many biological processes, including muscle contraction, the citric acid cycle, glycogen metabolism, release of neurotransmitters, vision, biological signal transduction and immune response. Synthetic systems that transport metal ions across lipid or liquid membranes are well known^{1–6}, and in some cases light has been used to facilitate transport⁷. Typically, a carrier molecule located in a symmetric membrane binds the ion from aqueous solution on one side and releases it on the other. The thermodynamic driving force is provided by an ion concentration difference between the two aqueous solutions, coupling to such a gradient in an auxiliary species, or photomodulation of the carrier by an asymmetric photon flux⁷. Here we report a different approach, in which active transport is driven not by concentration gradients, but by light-induced electron transfer in a photoactive molecule that is asymmetrically disposed across a lipid bilayer. The system comprises a synthetic, light-driven transmembrane Ca^{2+} pump based on a redox-sensitive, lipophilic Ca^{2+} -binding shuttle molecule whose function is powered by an intramembrane artificial photosynthetic reaction centre. The resulting structure transports calcium ions across the bilayer of a liposome to develop both a calcium ion concentration gradient and a membrane potential, expanding Mitchell’s concept of a redox loop mechanism for protons⁸ to include divalent cations. Although the quantum yield is relatively low (~ 1 per cent), the Ca^{2+} electrochemical potential developed is significant.

A redox loop mechanism for transmembrane ion transport is premised on differential binding of an ion by reduced and oxidized forms of a lipid-soluble transporter (shuttle) molecule. The transmembrane Ca^{2+} transport system is based on a redox loop involving the synthetic, lipophilic, membrane-soluble shuttle **1** (Fig. 1). Inspiration for **1** came from a suggestion that transmembrane Ca^{2+} transport in sponges might be based on a hydroquinone Ca^{2+} chelator⁹. Calcium binding by the hydroquinone form of **1** is expected, based on results for related 9,10-antraquinone and 9-anthrone derivatives⁶. This conclusion is supported by experiments on 2,5-dihydroxyacetophenone which, unlike **1**, has solubility in polar solvents. Calcium ion binding by this compound in aqueous solution at $\text{pH} = 7$ was investigated by using a calcium-specific electrode. Binding by Ca^{2+} of one or two hydroquinone anions with equilibrium constants of 820 M^{-1} and 75 M^{-1} , respectively, was detected. Binding was also studied using nuclear magnetic resonance (NMR) spectroscopy. Addition of excess CaCl_2 in D_2O to 2,5-dihydroxyacetophenone in deuterated acetonitrile containing one equivalent of KOH led to downfield shifts of the aromatic proton resonances, consistent with the binding of Ca^{2+} . A similar experiment with the quinone form resulted in no detectable shifts. We conclude that lipid-soluble hydroquinone **1** binds calcium ions, whereas the corresponding quinone does not.

We incorporated **1** in its hydroquinone form into the phospholipid bilayer of a liposome so as to serve as one component of a Ca^{2+}

pump. The proposed mechanism suggested by Fig. 1 stipulates that during a pumping cycle, a minimum of two molecules of the hydroquinone at the external surface of the membrane lose protons to the aqueous phase ($\text{pH} 7.5$) and bind Ca^{2+} . The resulting lipid-soluble complex diffuses across the membrane to the opposite interface. Oxidation of hydroquinone generates quinone, releasing Ca^{2+} to the aqueous phase inside the liposome. Diffusion of quinone and neutral hydroquinone (carrying two protons) to the initial side of the membrane, followed by reduction of the quinone, completes the redox loop. The result is cyclic transport of Ca^{2+} with no concurrent transport of hydrogen ions.

The redox power for the pump comes from light through artificial photosynthetic reaction centre **2**, which was employed in a previously reported light-powered transmembrane proton pump^{10,11}. This carotenoid (C), porphyrin (P), naphthoquinone (Q), molecular triad was inserted in a vectorial manner into the liposomal membrane with its naphthoquinone end near the external surface and its carotenoid functionality inside the hydrophobic portion of the bilayer¹¹. Excitation of **2** by visible light produces the $\text{C}^+-\text{P-Q}^-$ charge-separated state through photoinduced electron transfer. The carotenoid radical cation, a strong oxidizing agent, is responsible for conversion of the calcium-binding hydroquinone form of **1** to the quinone (either by sequential one-electron oxidations or by disproportionation reactions of the semiquinone intermediate), with release of Ca^{2+} to the inner liposomal volume. The naphthoquinone radical anion, located at the external surface of the liposome, is available for reduction of the quinone form of **1**.

Irradiation of the assembly diagrammed in Fig. 1 with light absorbed by the porphyrin leads to transmembrane Ca^{2+} transport, as indicated in Fig. 2. The internal Ca^{2+} concentration was monitored using the fluorescent dye Fluo-3 (ref. 12), which was located only inside the liposomes, and whose response was calibrated using liposomes containing known calcium concentrations. Figure 2 also shows a control experiment without illumination. When triad **2** or shuttle **1** was omitted, no calcium transport was detected. Calcium transport was not observed when **1** was replaced with a redox-sensitive proton shuttle that forms a transmembrane proton

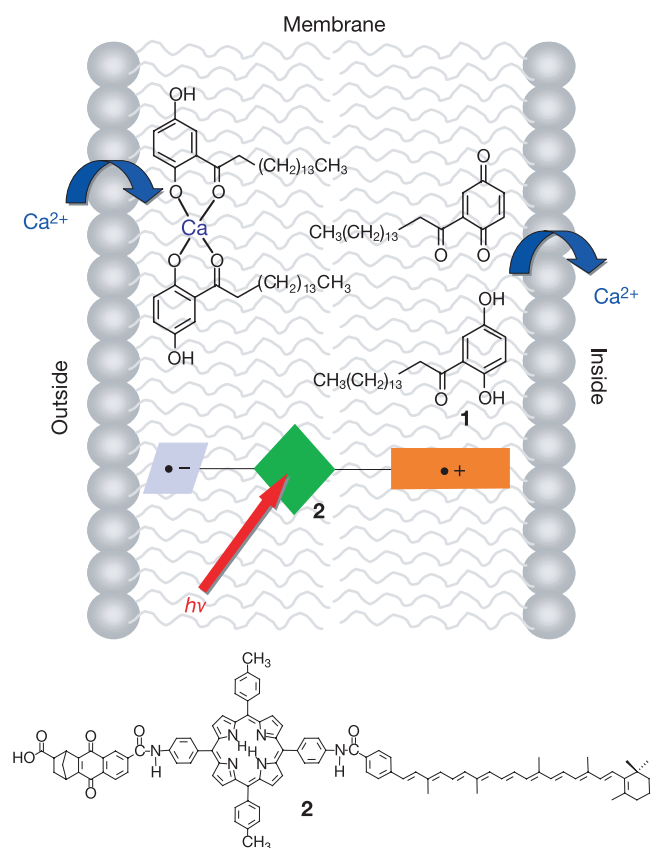


Figure 1 Schematic representation of a liposome-based, light-powered transmembrane Ca^{2+} pump. The carotenoid-porphyrin-naphthoquinone artificial reaction centre **2** crosses the membrane, with its hydrophilic quinone moiety near the external interface. Shuttle molecule **1** chelates Ca^{2+} at the external interface, diffuses across the membrane, and is oxidized by the carotenoid radical cation formed by photoinduced electron transfer in molecule **2**. After release of Ca^{2+} to the internal aqueous volume, the quinone form of **1** diffuses back across the membrane, where it can be reduced by the radical anion of **2** formed by photoinduced electron transfer.

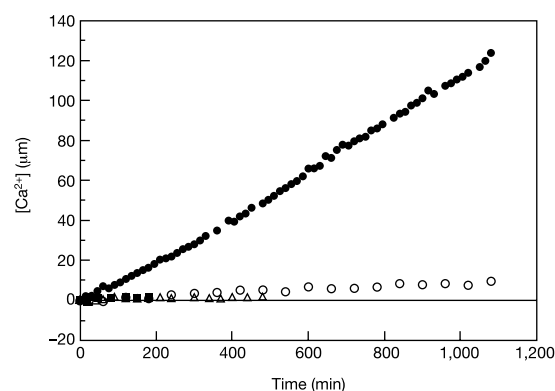


Figure 2 Transmembrane Ca^{2+} transport. The concentration of Ca^{2+} transported into the liposome interior as a function of time with (filled circles) and without (open circles) irradiation with 633-nm light was determined from the calibrated fluorescence intensity of the calcium indicator Fluo-3. Also shown are results for similar samples lacking the shuttle **1** (filled squares), and in which **1** has been replaced by a similar molecule bearing a methoxy group in the 5-position (open triangles). Reverse-phase evaporation liposomes prepared as previously described¹¹ were used. The organic lipid-forming solution contained 0.4 mol% of molecule **1**, and the aqueous solution ($\text{pH} 7.5$) contained 150 mM KCl, 10 mM HEPES buffer, and $100 \mu\text{M}$ Fluo-3. Purification of the liposomes and vectorial insertion of **2** were carried out as previously described¹¹, and CaCl_2 was then added to 1.0 mM. Actinic light was provided by a 3.6 mW, about 1 cm beam of 633-nm laser light. The sample in the cuvette (1.5 ml) was stirred.

pump¹⁰. Use of the ΔpH -sensitive dye 9-aminoacridine demonstrated that at $\text{pH} = 7.5$, in the presence or absence of added Ca^{2+} , **1** does not transport hydrogen ions across the membrane, with or without irradiation, under the conditions used for Ca^{2+} pumping. Methylation of the oxygen at the 5-position of **1** precludes formation of the quinone, increases the first oxidation potential (0.57 V versus 0.20 V (standard calomel electrode, SCE) for **1**) and abolishes Ca^{2+} pumping.

The suggested mechanism requires Ca^{2+} pumping to be electrogenic, as there is no net transmembrane transport of other charges. Introduction and calibration of the dye 8-anilino-1-naphthalenesulphonic acid, whose fluorescence yield is a function of membrane potential ($\Delta\psi$), and elimination of Fluo-3 allowed us to investigate this possibility. Illumination under conditions for Ca^{2+} pumping leads to formation of a membrane potential that is positive on the interior of the liposomes (Fig. 3). No $\Delta\psi$ is produced without actinic light, without **1** or **2**, or when **1** is replaced by its 5-methoxy analogue. Without added Ca^{2+} , and with the addition of a strong calcium chelator such as EDTA to the external aqueous solution to bind any adventitious calcium ions, a membrane potential is not produced. The membrane potential is discharged upon addition of 50 μM valinomycin, which permits potassium ions to flow out of the liposomes, or eventually upon standing in the dark.

In Fig. 2 the calcium concentration inside the liposome increases approximately linearly with irradiation time up to about 1,000 min. Because of the large binding constant of Fluo-3 for Ca^{2+} ($K_d = 390 \text{ nM}$ at $\text{pH} = 7.2$), there is never any significant amount of free Ca^{2+} inside the liposome, and therefore no free Ca^{2+} concentration opposing Ca^{2+} transport. In the absence of the Ca^{2+} -binding dye, however, the membrane potential studies may be used to obtain quantitative information about the performance of the Ca^{2+} pump. Figure 3 demonstrates that when no Ca^{2+} is added to the liposome interior before illumination, $\Delta\psi$ builds up with Ca^{2+} pumping, and maximizes at about 120 mV. At this point, the Ca^{2+} concentration inside the liposomes is still about 20 times lower than on the outside (Fig. 2). Even though the ion pump has not reversed the Ca^{2+} concentration gradient, potential energy is being stored as a membrane potential of about 120 mV. The fact that in the presence of Fluo-3, Ca^{2+} pumping continues unabated even after this potential limit is reached (Fig. 2) suggests that beyond this

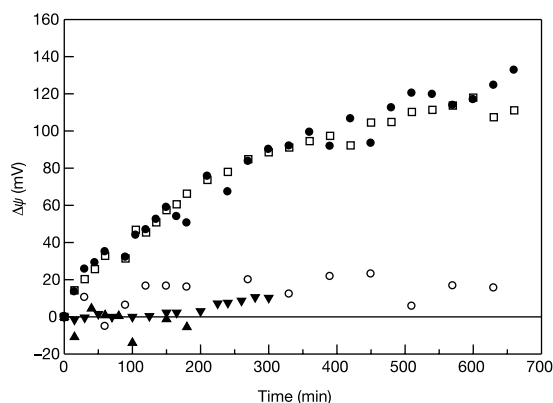


Figure 3 Light-induced formation of a membrane potential. The buildup of $\Delta\psi$ with irradiation of the liposomal system in Fig. 2 containing 1.0 mM Ca^{2+} in the external volume, and no added calcium or Fluo-3 in the internal liposomal volume, was determined from the calibrated fluorescence increase of the $\Delta\psi$ sensitive dye 8-anilino-1-naphthalenesulphonic acid (7 μM) (open squares). Also shown is the development of $\Delta\psi$ with (filled circles) and without (open circles) irradiation under the same conditions, but with 1.0 mM Ca^{2+} both inside and outside the liposomes. Control experiments include illumination by actinic light but without **2** (filled down triangles), or with replacement of **1** by its 5-methoxy analogue (filled up triangles).

limit, charge import by the Ca^{2+} pump is balanced by leakage of positive ions, or negative ions such as chloride.

Figure 3 also shows the buildup of $\Delta\psi$ when the initial concentration of Ca^{2+} both inside and outside the liposomes is 1.0 mM. The increase of $\Delta\psi$ with illumination occurs essentially as it does when calcium is excluded from the interior, and no $\Delta\psi$ is generated in the absence of actinic light. Thus Ca^{2+} can be pumped across the membrane even against a Ca^{2+} concentration gradient and a membrane potential. Because the amount of Ca^{2+} pumped ($\sim 50 \mu\text{M}$) is small relative to the ambient concentration, the electrochemical potential built up is mainly $\Delta\psi$. This experiment unambiguously demonstrates that the transmembrane ion pump stores some of the light energy harvested by the artificial reaction centre as electrical and chemical potential energy.

The $\Delta\psi$ measurements may be used to estimate the quantum yield of Ca^{2+} transport, $\Phi_{\text{Ca}^{2+}}$, assuming that the only electrogenic process is the import of two positive charges per ion. The initial rate of $\Delta\psi$ increase ($d\Delta\psi_{\text{Ca}^{2+}}/dt$) was compared with the initial rate of $\Delta\psi$ increase in an artificial proton pump/ATP producing system ($d\Delta\psi_{\text{H}^+}/dt$) described earlier. The quantum yield of the proton pump was previously estimated¹¹ as 0.6. The actinic light level was such that the rate of $\Delta\psi$ generation was linear with intensity for both pumps. Under these conditions, $(d\Delta\psi_{\text{H}^+}/dt)/(d\Delta\psi_{\text{Ca}^{2+}}/dt)$ is proportional to the ratio of the quantum yields, giving $\Phi_{\text{Ca}^{2+}} \approx 0.01$. This method does not require knowledge of the size or number of liposomes, as long as these quantities and the number of artificial reaction centres per liposome are the same in both cases.

The results reported here are consistent with the proposed mechanism for Ca^{2+} translocation suggested above. However, the details of the transport are not as yet fully understood. In particular, the stoichiometry of Ca^{2+} binding, the exact oxidation state of **1** at the time of Ca^{2+} release, and the detailed mechanism for formation of the quinone form of **1** are unknown. Under the conditions of our experiment, a $\Delta\psi$ is produced in the presence of Ca^{2+} , and not in its absence. This demonstrates that there is no competitive transmembrane transport of other ions in either direction before reaching the limiting $\Delta\psi$. We note that **1** is not observed to function as a proton pump in the presence or absence of Ca^{2+} . In contrast to the earlier-reported proton pump¹⁰, shuttle **1** was introduced into the system only in the hydroquinone form, which does not bind additional protons. The facile reduction of the quinone form of **1**, the pKa values of its various redox states, and their membrane solubility properties may play a role in the lack of proton transport.

These results demonstrate that a light-powered artificial photosynthetic reaction centre can be coupled to endergonic transmembrane Ca^{2+} transport by a redox loop to store energy as a combination of electrical and chemical potential. Although it is biomimetic only in the broadest sense, the system illustrates how various elements of biological energy transduction may be abstracted and combined in nanoscale synthetic constructs that perform interesting and potentially useful functions. □

Received 18 July; accepted 10 October 2002; doi:10.1038/nature01209.

- Bartsch, R. A. & Way, J. D. *Chemical Separations with Liquid Membranes* (American Chemical Society, Washington, 1996).
- Hirose, T., Baldwin, B. W. & Wang, Z. H. Kemp's triacid derivatives as versatile divalent metal ion transport agents and their utilization as chromoionophores. *Recent Res. Dev. Pure Appl. Chem.* **2**, 527–546 (1998).
- de Gyves, J. & de Miguel, E. R. Metal ion separations by supported liquid membranes. *Indust. Eng. Chem. Res.* **38**, 2182–2202 (1999).
- Lamrabte, A., Janot, J. M., Bienvenue, E., Momenteau, M. & Seta, P. Photoinitiated vectorial transmembrane electron transfer in bilayers sensitized by a face to face triporphyrin acting as a molecular electronic device. Amplification due to ionic coupling. *Photochem. Photobiol.* **54**, 123–126 (1991).
- Zhao, Z.-G. & Tollin, G. Chlorophyll photosensitized electron transfer reactions in lipid bilayer vesicles: Generation of proton gradients across the bilayer coupled to quinone reduction and hydroquinone oxidation. *Photochem. Photobiol.* **55**, 611–619 (1992).
- Dadfarnia, S., Shamsipur, M., Tamaddon, F. & Sharghi, H. Extraction and membrane transport of metal ions by some synthetic 9,10-anthraquinone and 9-anthrone derivatives. A selective system for calcium transport. *J. Membr. Sci.* **78**, 115–122 (1993).

7. Longin, T. L., Goyette, M. L. & Koval, C. A. Liquid membranes with light switches. *Chem. Innov.* **31**, 23–30 (2001).
8. Mitchell, P. Chemiosmotic coupling in oxidative and photosynthetic phosphorylation. *Biol. Rev. Camb. Phil. Soc.* **41**, 445–502 (1966).
9. Sullivan, B. W. & Faulkner, D. J. *New Perspectives in Sponge Biology* (ed. Rützler, K.) 45–50 (Smithsonian Institution Press, Washington, 1990).
10. Steinberg-Yfrach, G. *et al.* Artificial photosynthetic reaction centers in liposomes: Photochemical generation of transmembrane proton potential. *Nature* **385**, 239–241 (1997).
11. Steinberg-Yfrach, G. *et al.* Light-driven production of ATP catalysed by F₀F₁-ATP synthase in an artificial photosynthetic membrane. *Nature* **392**, 479–482 (1998).
12. Minta, A., Kao, J. P. Y. & Tsien, R. Y. Fluorescent indicators for cytosolic calcium based on rhodamine and fluorescein chromophores. *J. Biol. Chem.* **264**, 8171–8178 (1989).

Acknowledgements This research was supported by the US Department of Energy and the Harrington Arthritis Research Center.

Competing interests statement The authors declare that they have no competing financial interests.

Correspondence and requests for materials should be addressed to D.G. (e-mail: gust@asu.edu).

Climate change in the North Pacific region over the past three centuries

G. W. K. Moore*, Gerald Holdsworth† & Keith Alverson‡

* Department of Physics, University of Toronto, Toronto, Ontario M5S 1A7, Canada

† Arctic Institute of North America, University of Calgary, Calgary, Alberta T2N 1N4, Canada

‡ PAGES International Project Office, Bern CH-3011, Switzerland

The relatively short length of most instrumental climate records restricts the study of climate variability^{1,2}, and it is therefore essential to extend the record into the past with the help of proxy data. Only since the late 1940s have atmospheric data been available³ that are sufficient in quality and spatial resolution to identify the dominant patterns of climate variability, such as the Pacific North America pattern^{4,5} and the Pacific Decadal Oscillation⁶. Here we present a 301-year snow accumulation record from an ice core at a height of 5,340 m above sea level—from Mount Logan, in northwestern North America. This record shows features that are closely linked with the Pacific North America pattern for the period of instrumental data availability. Our record extends back in time to cover the period from the closing stages of the Little Ice Age to the warmest decade in the past millennium⁷. We find a positive, accelerating trend in snow accumulation after the middle of the nineteenth century. This trend is paralleled by a warming over northwestern North America which has been associated with secular changes in both the Pacific North America pattern and the Pacific Decadal Oscillation.

Mount Logan, located in the heavily glaciated Saint Elias mountains of the Yukon, is the highest mountain in Canada and is situated in a region of climatological importance. It is located at the end of the major North Pacific storm track⁸ along the main atmospheric pathway by which water vapour enters northwestern Canada⁹. In 1980, a 103-m ice core was retrieved from a high elevation site (5,340 m above sea level) on the mountain. Recent shallow coring and snow-pit sampling at the site have extended the ice-core record to the year 2000. Stratigraphic techniques^{10–12} allow for the retrieval of annual snow accumulation data extending from 1693 to 2000. The section before 1736 did not have annual snow accumulations assigned throughout owing to a lack of reliable seasonal indicators¹⁰. It has been shown that the annual snow

accumulation time series from this ice core contains information on circulation and temperature patterns throughout the North Pacific region^{13,14}.

Figure 1 shows the updated snow accumulation time series from the Mount Logan site over the period 1700–2000. The time series exhibits variability on both the interannual as well as interdecadal timescales¹³. Furthermore, Fig. 1 indicates that snow accumulation at the site has increased over this period, with much of the increase occurring during the latter half of the record. To assess the statistical significance of this increase, we tested the validity of the null hypothesis that the trend in annual snow accumulation at the site, obtained with the least-squares method, is indistinguishable from zero. To counteract the known tendency of geophysical time series to exhibit elevated power at low frequencies¹⁵, we assumed that the regression residuals are temporally correlated. As a result, we used a reduced effective sample size, which is a function of the lag-1 (year) autocorrelation of the regression residuals, in the test of statistical significance¹⁶. This test showed that from 1736–1850 the trend was not significantly different from zero. The lack of any trend during this period is also consistent with the data from 1700–35. Over the more recent portion of the record, from 1851 onwards, the trend is significant at the 95% confidence level. Furthermore, there is evidence for a recent acceleration in the rate of snow accumulation. In Table 1, we show that over the period 1948–2000, the trend was approximately four times as large as over the period 1851–2000. An even more rapid increase has occurred over the period 1976–2000.

Given the results presented in Fig. 1 and Table 1, we seek to identify trends in the region that have contributed to the observed increase in snow accumulation at the site. Figure 2 shows the trend in winter mean surface temperature in the North Pacific region as contained in the HADCRUTv data set¹⁷. Results are shown for the entire period of this data set, 1870–1999, as well as for the period 1948–99. Over the entire period, the dominant feature in this field is a warming in northwestern North America and the adjoining northeast Pacific Ocean. In addition to this feature, over the past 52 years there has also been a cooling over the North Pacific. There is also a marked increase in the rate of warming over North America in recent years^{17,18}.

Figure 3 shows the regression of the winter mean 500-mbar geopotential height, vertically integrated moisture transport and 1,000–500-mbar thickness fields from the National Center for Environmental Prediction (NCEP) reanalysis^{3,19} for the period 1948–2000 with the annual snow accumulation time series from the Mount Logan ice core. The 500-mbar pressure surface is located at the approximate elevation of the ice core site and its height is

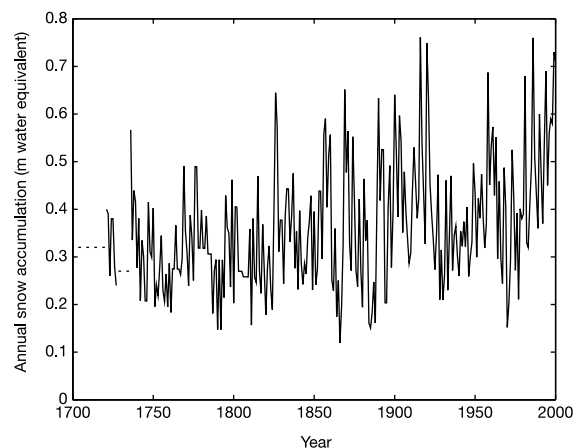


Figure 1 Annual snow accumulation (m water equivalent) at the Mount Logan site 1700–2000. Data in the pre-1736 era that is not annually resolved is indicated by the dashed lines.